Analytical and Bioanalytical Chemistry
https://doi.org/10.1007/s00216-020-03032-6

RESEARCH PAPER

Cu_2O-mediated assembly of electrodeposition of Au nanoparticles onto 2D metal-organic framework nanosheets for real-time monitoring of hydrogen peroxide released from living cells

Sha Chen[1] · Peng Zhao[1] · Liuyi Jiang[1] · Shiying Zhou[1] · Jilin Zheng[1] · Xiaogang Luo[1] · Danqun Huo[1] · Changjun Hou[1,2]

Received: 22 August 2020 / Revised: 19 October 2020 / Accepted: 27 October 2020

Abstract

The development of metal nanoparticles (MNP) combined with a metal-organic framework (MOF) has received more and more attention due to its excellent synergistic catalytic ability, which can effectively broaden the scope of catalytic reactions and enhance the catalytic ability. In this work, we developed a novel ternary nanocomposite named Cu_2O-mediated Au nanoparticle (Au NP) grown on MIL-53(Fe) for real-time monitoring of hydrogen peroxide (H_2O_2) released from living cells. First, Cu_2O-MIL-53(Fe) was prepared by redox assembly technology, which provided the growth template, and active sites for $AuCl^{4-}$. Au@Cu_2O-MIL-53(Fe)/GCE biosensor was prepared by further loading nano-Au uniformly on the surface of Cu_2O by electrochemical deposition. Compared to individual components, the hybrid nanocomposite showed superior electrochemical properties as electrode materials due to the synergistic effect between AuNPs, Cu_2O, and MIL-53(Fe). Electrochemical measurement showed that the Au@Cu_2O-MIL-53(Fe)/GCE biosensor presented a satisfactory catalytic activity towards H_2O_2 with a low detection limit of 1.01 μM and sensitivity of 351.57 μA mM^{-1} cm^{-2} in the linear range of 10–1520 μM. Furthermore, this biosensor was successfully used for the real-time monitoring of dynamic H_2O_2 activated by PMA released from living cells. And the great results of confocal fluorescence microscopy of the co-culture cells with PMA and Au@Cu_2O-MIL-53(Fe) verified the reliability of the biosensor, suggesting its potential application to the monitoring of critical pathological processes at the cellular level.

Keywords NPs-MOFs · Hydrogen peroxide · Electrochemical sensor · Living cells

Introduction

Hydrogen peroxide (H_2O_2) is a relatively stable and easier detectable molecule in ROS cluster. Generally, H_2O_2 production and elimination can reach a balance under normal physiological conditions. However, such balance is broken in cancer cells, resulting in oxidative stress that interferes with the cell's function [1]. The H_2O_2 will rise dramatically in cancer cells and diffuse outside of the living cell. Therefore, it is critically important to realize real-time monitoring H_2O_2 released by living cells for better understanding the pathological processes of cancer cells. However, it needs to overcome the problems of quick diffusion, low concentration, and easy interference of H_2O_2 in the microenvironment of the cell. So far, various methods have been developed for detection including chemiluminescence [2], fluorescence nanoprobe [3], photoelectron-chemical [4], electron spin resonance [5], and electrochemical sensing [6]. Among them, the electrochemical sensing has the advantages of being relatively portable and

Supplementary Information The online version contains supplementary material available at https://doi.org/10.1007/s00216-020-03032-6.

✉ Xiaogang Luo
luosteel@cqu.edu.cn

✉ Danqun Huo
huodq@cqu.edu.cn

✉ Changjun Hou
houcj@cqu.edu.cn

[1] Key Laboratory for Biorheological Science and Technology of Ministry of Education, State and Local Joint Engineering Laboratory for Vascular Implants, Bioengineering College of Chongqing University, Chongqing 400044, China

[2] Chongqing Key Laboratory of Bio-perception & Intelligent Information Processing, School of Microelectronics and Communication Engineering, Chongqing University, Chongqing 400044, China

Published online: 07 November 2020

has high sensitivity and selectivity. Especially, its amperometric technique provides rapid temporal resolution for highly sensitive tracking and real-time cell secretion monitoring. However, the performance of a typical electrochemical enzyme-based sensor is usually affected by the inferior reproducibility and stability of enzymes through different environmental [7]. To avoid those problem, various non-enzymatic electrochemical sensors fabricated by electrocatalytic nanomaterials including conducting polymer [8–10], metals and their compounds [11–13], graphene composites [14–16], and metal-organic framework (MOFs) [17–19] have been developed for H_2O_2 detection.

Meanwhile, as there is increasing interest in the cellular metabolic processes of the disease, more and more attention is focused on monitoring H_2O_2 in real samples. In the reported researches, it mainly involves serum spike and cell experiment. And in cell experiments, the performance of the sensor is usually shown by comparing the electrochemical signals containing cells and stimuli (with or without catalase) and only containing stimuli. The commonly used stimuli include PMA [20], fMLP [21], AA [22], and LPS [23], which are all chemicals that can stimulate cells to secrete extracellular hydrogen peroxide. At the same time, Lilian et al. [21] explored the effect of different concentrations of fMLP and found that the maximum H_2O_2 release in 2×10^6 4T1 cell solution was assumably estimated as 25 nM. Hongxia et al. [24] compared the amount of H_2O_2 released by different types of cells, and verified the tendency of cancerous cells to generate more H_2O_2 due to their rapid oxygen metabolism. However, how to design a novel electrochemical H_2O_2 sensor with good biocompatibility and better catalytic performance for cell experiments is still a challenge.

Metal-organic frameworks (MOFs) are framework structures composed of cross-linking organic ligands and metal ion nodes [25]. A large number of electrochemical sensors based on MOFs for H_2O_2 detection have been successfully fabricated, such as ZIF-67/CNFs [26], Cu-MOF/graphene [17], Au/Fe-MOF [27], Pt@P-MOF(Fe) [28], and CoFe-PBA/Co-ZIF/NF [29]. Unfortunately, their catalytic activity is limited by unsaturated metal cations [30] and/or modified groups in organic ligands [31]. To broaden the application of MOFs in catalysis, researchers tried to functionalize the MOFs with incorporating conductive and catalytically active materials which includes conducting polymers [8], carbon materials [14], and noble metal (Au, Pd, Pt) nanoparticles [27]. Among these materials, metal nanoparticles (NPs) rapidly gain a huge amount of interest.

The application of NP-MOF composite to the electrocatalytic detections has been confirmed to exhibit great potential. Ling et al. reported a new biomimetic redox nanozyme, Pt nanoparticles grown on P-MOF(Fe), which was used to detect metabolites released by HeLa cells [28]. Ma et al. synthesized a nanocomposite Ag nanoparticles on 2D Cu-TCPP(MOF) with an extended linear response range towards H_2O_2 [32]. Generally, NP-MOFs can be synthesized by loading NPs on the pores or surfaces of MOFs through in situ reduction [33, 34] or assembling MOFs to surround prefabricated NPs in a MOF reaction solution [35]. However, there is extremely rare work about metal oxide-mediated progressive assembly of nanoparticles onto MOFs for catalytic reactions.

Herein, we construct a non-enzyme sensor of Cu_2O-mediated growth of Au nanoparticles (Au NPs) on 2D MIL-53 (Fe) for real-time detection H_2O_2 released from living cells (Scheme 1). Compared with electrostatic interaction-based method that directly reduces the nanoparticles to the surface of MOF material, the Cu_2O-mediated stepwise assembly method used in this work provided a more stable chemical bonds for the combination. On one hand, Au NP heterogeneous nanospheres loaded on 2D sheets possessed better electrochemical properties due to the synergistic effect. On the other hand, the 2D porous structure of MIL-53(Fe) with the large surface area can provide NPs with space-constrained inherent conditions to avoid agglomeration, which was beneficial to the stability and catalytic activity. Meanwhile, their pores could work as a molecular sieve to enrich hydrogen peroxide to improve the efficiency of the reaction with active sites.

Materials and methods

Reagents

Ferric chloride hexahydrate ($FeCl_3 \cdot 6H_2O$), hydrogen peroxide H_2O_2 (30%), and copper(II) chloride dehydrates ($CuCl_2 \cdot$

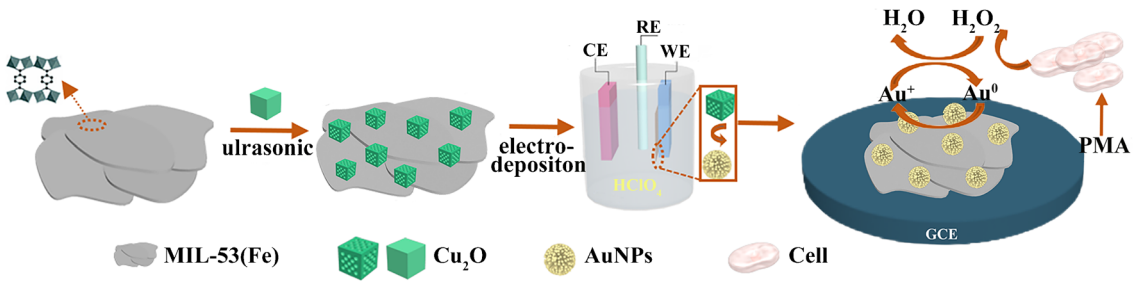

Scheme 1 Diagrammatic sketch of the preparation process of Au@Cu_2O-MIL-53(Fe) for real-time monitoring of H_2O_2 released from the living cells

$2H_2O$) were purchased from Chongqing Chuan Dong Chemical Group (China). Glucose (Glu), uric acid (UA), ascorbic acid (AA), dopamine hydrochloride (DA), gold chloride trihydrate ($HAuCl_4 \cdot 3H_2O$), terephthalic acid (H_2BDC), N,N-dimethylformamide (DMF), catalase (2000–5000 U/mg), phorbol 12-myristate-13-acetate (PMA), and human serum were purchased from Sigma-Aldrich (Shanghai, China). Cysteine (Cys) was bought from Tianjin Guangfu Fine Chemical Research Institute (China). Calcein-AM (green) and PI (red) were obtained from Beyotime Biotechnology (China). The A549 cells used in the study were obtained from Beijing Beina Chuanglian Institute of Biotechnology (China). Deionized water (DI, 18 MΩ, America) was used in all experiments and produced by a Millipore Direct-Q water system.

Apparatus

The surface morphology was examined by field emission scanning electron microscope (FE-SEM, JEOL-6300F, Japan). Crystal structures were analyzed using X-ray (XRD, Maxima-X XRD-7000, Japan) diffraction with radiation. The elemental valence change and relative content were obtained by X-ray photoelectron spectroscopy (XPS, Japan). The energy dispersive spectroscopy (EDS) and internal microstructure images (TEM) were obtained at 150 kV by transmission electron microscopy (JEOL-2100, Japan). All the electrochemical experiments were performed on the electrode system (CHI 660E Electrochemical Workstation, China), which included Ag/AgCl, platinum wire, and glassy carbon electrode (GCE). Phosphate-buffered saline (PBS, 0.01 M) was applied as an electrolyte (PH 7.4). The buffer was deoxygenated with nitrogen (99%) for all electrochemical measurements.

Preparation of Cu_2O-MIL-53 (Fe)

To prepare cubic Cu_2O, 0.170 g $CuCl_2 \cdot 2H_2O$ was dissolved in 100 mL water. Then NaOH solution (2 M, 10 mL) was dropped into the mixture with vigorous stirring at 55 °C until the brown liquid. After stirred for 0.5 h, AA solution (0.6 M, and 10 mL) was added and stirred for another 3 h. After centrifugation, the mixture was washed with distilled water and ethanol thrice, and freeze-dried.

MIL-53(Fe) was hydrothermally synthesized by a one-step method. 0.272 g $FeCl_3 \cdot 6H_2O$ and 0.166 g H_2BDC were dissolved in 25 mL DMF, respectively. And then the mixture was introduced into a 100-mL Teflon-lined steel autoclave and placed in a 150 °C oven for 12 h. After centrifugation, the mixture was washed thoroughly with DMF and ethanol thrice, and freeze-dried.

Cu_2O-MIL-53 (Fe) nanocomposites were prepared by dissolved Cu_2O and MIL-53(Fe) in 1 mL Nafion solution. The total mass was controlled at 2 mg with the same treatment, and the mass ratio of Cu_2O and MIL-53(Fe) was 1:2, 1:3, 1:1, 2:1, and 3:1 respectively.

Fabrication of Au@Cu_2O-MIL-53 (Fe)/GCE

The surface of GCE was polished with 0.3 and 0.05 μm alumina slurries in succession and thoroughly rinsed with distilled water. After sonication and drying with nitrogen, smoothed GCE was obtained. The as-prepared Cu_2O/MIL-53 (Fe) suspensions were dropped evenly onto the sensing area of the GCE. After the surface forming a uniform thin film around 8 h in room temperature, the electrochemical deposition of Au NPs was performed in a $HAuCl_4$ (2 mM, 5 mL) solution using an amperometric method with an applied potential of − 0.2 V for 200 s. The electrochemical deposition of Au NPs was performed in a $HAuCl_4$ (2 mM, 5 mL) solution using an amperometric method at an applied potential of − 0.2 V for 200 s. There was a reaction in the solution: $2AuCl^4{}^- + 3Cu_2O + 6H^+ = 2Au + 6Cu^{2+} + 8Cl^- + 3H_2O$. To explore the influence of different $HAuCl_4$ concentrations on the morphology, nanomaterials were prepared by depositing at 1 mM, 1.5 mM, 2.5 mM, and 3 mM.

Real-time electrochemical monitoring of living cellular H_2O_2

A549 cells were nurtured in 5 mL Hyclone Classical Liquid Media of Dulbecco's Modified Eagle Medium/Nutrient Mixture F-12 (DMEM/F-12, USA), which was supplied with 10% fetal bovine serum (Solarbio, China) and 1% penicillin-streptomycin (Solarbio, China). The cell culture flask was cultured in a 95% humidified environment at 37 °C with 5% CO_2. The cells took 48 h to grow to 90% confluence. Afterward, 2×10^5 cells measured by a hemocytometer were suspended in 5 mL of PBS electrolyte, and Au@Cu_2O-MIL-53(Fe)/GCE was placed into it for H_2O_2 monitoring. PMA (200 ng mL^{-1}, 10 μL) was injected to as stimulant to detect the production of H_2O_2 by the cells in real-time. Two groups of controls were established, and both groups received the same amount of PMA added to PBS. One control group contained no cells, whereas the other group had cells and enzymes.

Results and discussion

Characterization of Au@Cu_2O-MIL-53(Fe)

The morphologies, microstructures, and valence change of Au@Cu_2O-MIL-53 (Fe) were studied by FE-SEM, TEM, XRD, and XPS method. Figure 1a shows the MIL-53(Fe) 2D stacked sheet structure. Figure S2a (see Electronic Supplementary Material, ESM) shows the cubic Cu_2O with

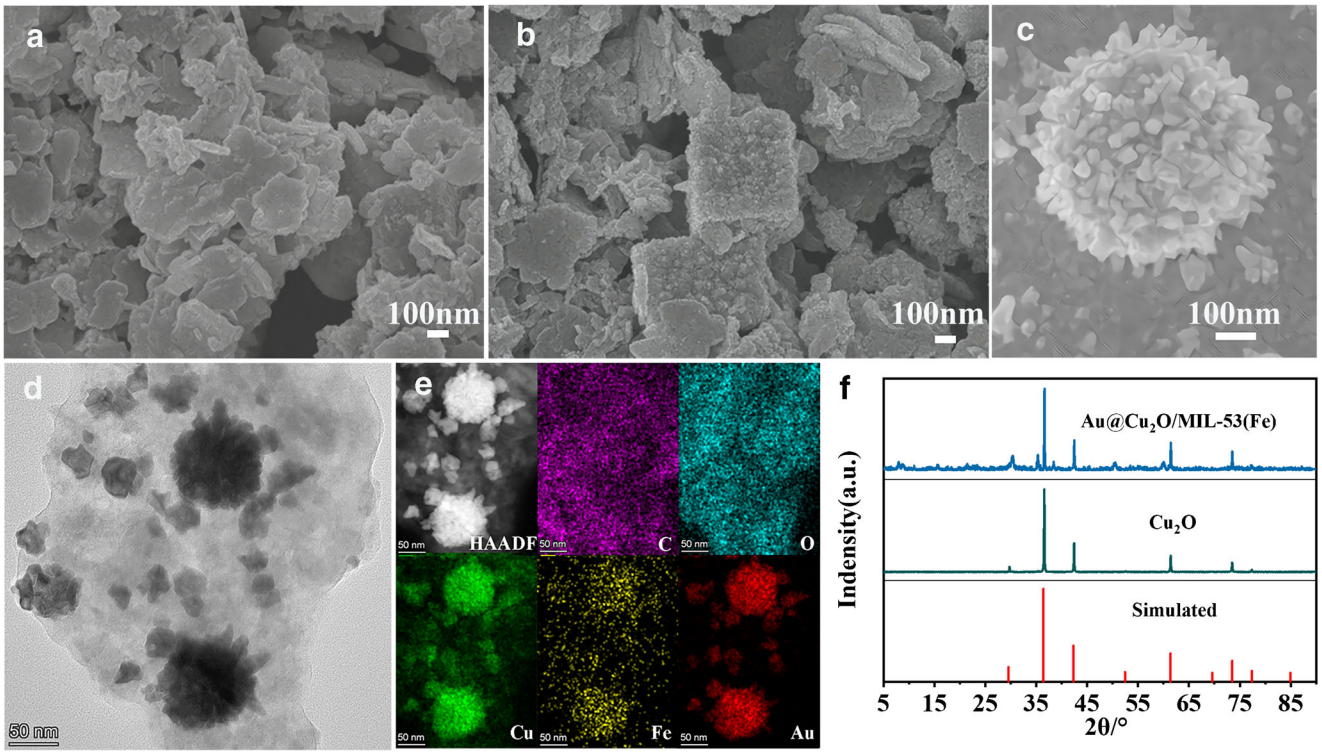

Fig. 1 FE-SEM images of **a** MIL-53(Fe), **b** Cu_2O-MIL-53(Fe), and **c** Au@Cu_2O-MIL-53(Fe). **d** TEM image, **e** EDS element mapping, and **f** XRD of Cu_2O and Au@Cu_2O-MIL-53(Fe) composites

smooth surfaces. After ultrasonically mixing MIL-53(Fe) with Cu_2O in 1:1 ratio, Cu_2O-MIL-53(Fe) was assembled by redox reaction between Cu_2O and MIL-53(Fe). As shown in Fig. 1b, the surface of Cu_2O-MIL-53(Fe) presented uniform NP throughout, indicating the reaction between Cu_2O and MOF. The metal connectors of MIL-53(Fe) have weak connection with its organic cross-linking agent, which provides a weak octahedral ligand field environment for Fe^{3+} [36] so that the metal ions in MOF are exposed to the coordinated unsaturated sites on the surface of MOFs. Thus, Fe^{3+} could redox-react with Cu_2O spontaneously from the perspective of thermodynamics [37]. One-step low potential deposition was used to reducing the metal ions to a metal-type solid state. Figure S2 (see ESM) shows the morphology and size of nanoparticles controlled by the concentration of $HAuCl_4$. As the concentration grew higher, the nanoparticles grew bigger. In the concentration of 2 mM $HAuCl_4$, the best morphology of uniform circle and moderate size was obtained. After electrochemical deposition with Cu_2O-MIL-53(Fe) in 2 mM $HAuCl_4$, Au nanoclusters formed from the Cu_2O surface bonded to the MOF surface (Fig. 1c) forming Au@Cu_2O-MIL-53(Fe). Here, the Cu_2O worked as a temple for Au nanoparticles to grow oriented into nanospheres with the basic skeleton of Cu_2O (ESM Fig. S1).

The Au@Cu_2O-MIL-53(Fe) was observed as flower-like nanospheres in Fig. 1c with a size about 500 nm (ESM Fig. S3c). And these nanospheres were composed of many small cubes of uniform size about 30 nm, which could effectively expand the specific surface area of the material to facilitate electron transmission. After modified by AuNPs over 7 days, the small nanoparticles making up the nanospheres turned to round from square (ESM Fig. S3). Meanwhile, after comparing the nanosphere sizes, it was found that the nanospheres became more uniform small particles over 7 days. This phenomenon was attributed to the continuous oxidation of Cu_2O inside the nanoparticles, so the large nanoparticles were divided into small particles. More detailed structures were observed through TEM (Fig. 1d) and EDS element mapping analysis (Fig. 1e). The samples containing Au, Cu, and Fe elements were mainly concentrated in the nanospheres, indicating that the composite nanomaterial was heterogeneous nanomaterial formed by the interaction between NPs and MOF. The sharp characteristic diffraction peaks of the Cu_2O XRD (Fig. 1f) at 30.2 °, 36.6 °, 42.5 °, 61.4 °, and 73.5 ° were indexed to (110), (111), (200), (220), and (311) planes, respectively [38], which confirmed the existence of cubic Cu_2O crystalline (JCPDS card No. 05-0667). The comparison of XRD of Au@Cu_2O-MIL-53(Fe) showed the same characteristic peaks, implying the successful synthesis of Cu_2O directional growth strategy to assemble Au NPs on MIL-53 (Fe).

XPS characterization was used to determine the elemental valence change and relative content of assembly of step by step redox reactions for Au NPs and MOF composite. The Fe 2p, Cu 2p, Au 4f, and O1s images of Au@Cu_2O-MIL-53 (Fe)

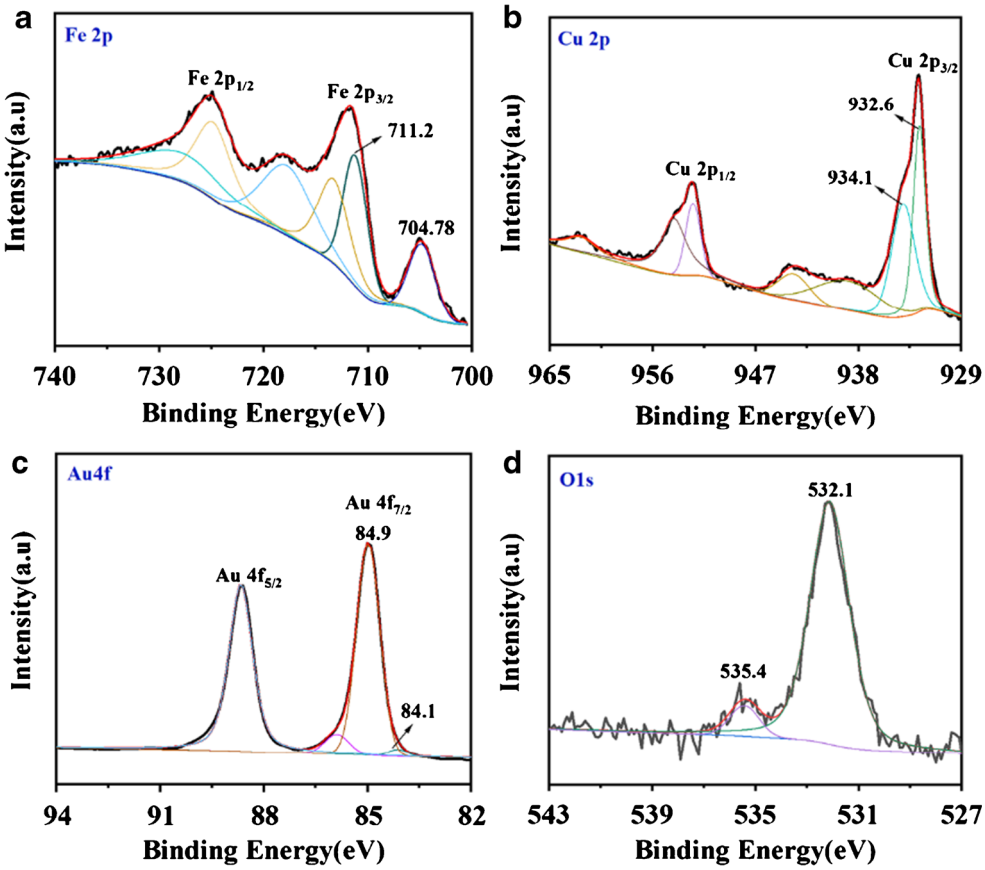

Fig. 2 The peak fitting graph of **a** Au 4f, **b** Cu 2p, **c** Fe 2p, and **d** O1s XPS spectra of an Au@Cu_2O-MIL-53(Fe)

were demonstrated in Fig. 2. And the related peak positions and abundance calculations were illustrated in Table 1. The Fe 2p peak position of 724.8 eV was assigned to Fe 2p1/2, and 711.2 eV (Fig. 2a) was assigned to Fe 2p3/2 (Fig. 2a) [39], corresponding to the MIL-53(Fe) [40, 41]. Another two distinct peaks were observed at 717.7 and 704.8 eV, corresponded to the Fe^0 [42], indicating that Fe^{3+} was reduced in composite. In Fig. 2b, the main Cu $2p_{3/2}$ peaks located at 934.1 eV illustrated that Cu^+ had been oxidized to Cu^{2+}. The formation of Cu^{2+} was achieved by Cu_2O reacting with oxygen in the air, the Fe^{3+} of MOF, and $HAuCl_4$. As for Au 4f (Fig. 2c), the peaks of Au $4f_{5/2}$ and $4f_{7/2}$ located at 88.6 and 84.9 eV corresponded to the $Au^{\delta+}$ ($0 < \delta < 1$) species at a large proportion [43, 44], whereas the others were assigned to metallic Au^0. The formation of $Au^{\delta+}$ species resulted from metallic Au NP bonding with the oxygen species of the support, and these species were located at the interfaces with the particles in contact of the support [45]. As reported, gold in this valence state had a more active catalytic activity [46], which benefits the insertion of oxygen atoms in the redox process [47]. The high-resolution XPS spectrum of the O1s (Fig. 2d) that could be fitted by peaks at binding energies of around 532.12 eV was attributed to the surface oxygen species bound by metal atoms of Fe-O and Cu-O. In addition, the peak appeared at 535.42 eV corresponded to O-H in H_2O_2. Compared with the standard spectrogram O1s, the binding energy increased, proving that oxidation-reduction reaction occurred. The total peak information was placed in Fig. S4 (see ESM).

Table 1 Peak position and abundance of elements of different valences

Orbital	Valence state	Binding energy (eV)	Ratio (%)
$Fe2p_{3/2}$	Fe^{3+}	711.2	67.7
	Fe^0	704.8	32.2
$Cu2p_{3/2}$	Cu^{2+}	934.1	61.9
	Cu^+	932.6	38.1
$Au4f_{3/2}$	$Au^{\delta+}$	84.97	94.2
	Au^0	84.12	5.8

Electrochemical performance of Au@Cu_2O-MIL-53(Fe)/GCE

Cyclic voltammetry (CV) was employed to investigate the electrochemical properties of different GCE in a range from −0.2 to +0.6 V at a scan rate of 50 mV s^{-1} in 5 mM Fe $(CN)_6^{3-/4-}$ solution containing 0.1 M KCl (Fig. 3a). When modified with Cu_2O, MIL-53(Fe), Cu_2O-MIL-53(Fe), the redox peak current decreased lightly, indicating the poor conductivity. After electrodeposition modification, the

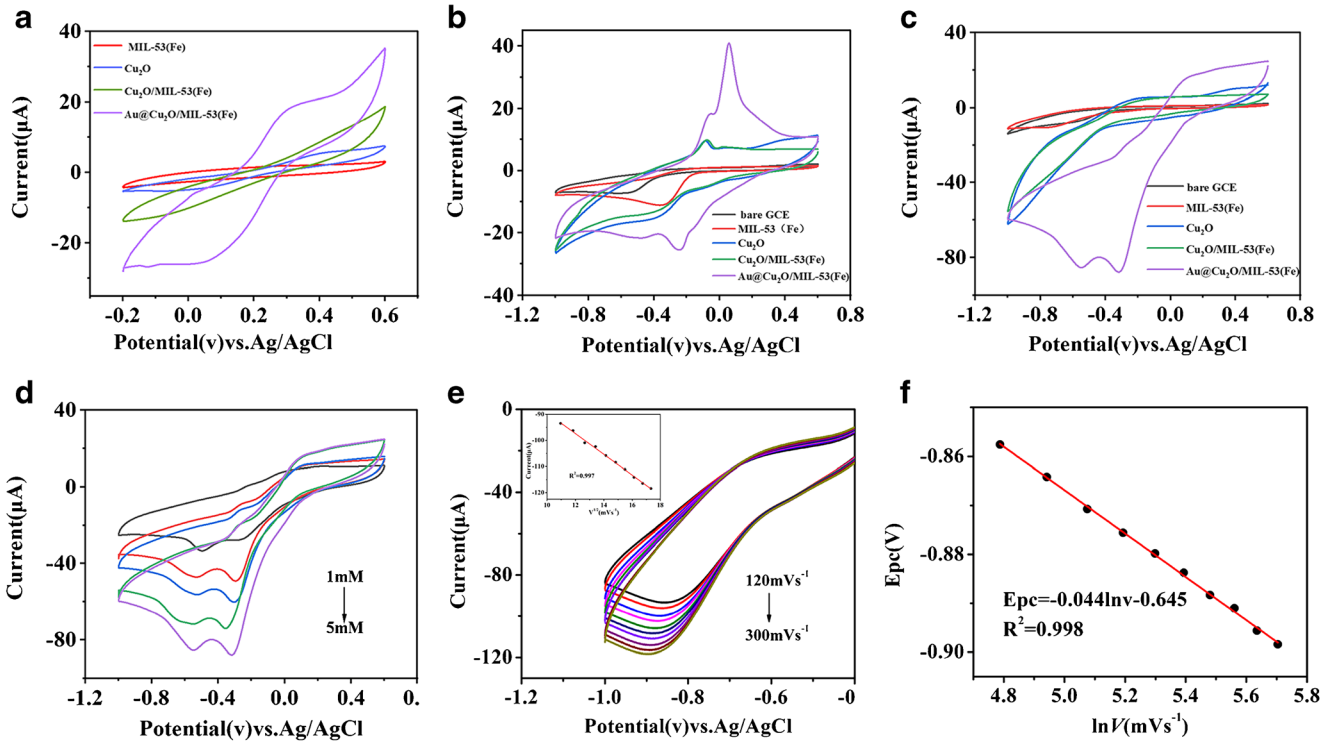

Fig. 3 CV of MIL-53(Fe)/GCE, Cu_2O/GCE, Cu_2O-MIL-53(Fe)/GCE, Au@Cu_2O-MIL-53(Fe)/GCE at a scan rate of 50 mV s^{-1} in **a** 5 mM $Fe(CN)_6^{3-/4-}$ solution containing 0.1 M KCl, in N_2-saturated 0.01 M PBS (pH 7.4) solution with **b** the absence and **c** the presence of 5 mM H_2O_2. **d** CV of Au@Cu_2O-MIL-53(Fe)/GCE a scan rate of 50 mV s^{-1} in different concentrations of H_2O_2 N_2-saturated 0.01 M PBS (pH 7.4) solution. The H_2O_2 concentrations is 1 mM, 2 mM, 3 mM, 4 mM, and 5 mM, respectively. **e** CV of Au@Cu_2O-MIL-53(Fe)/GCE in different scan rate in N_2-saturated.0.01 M PBS (pH 7.4). Scan rate in the range of 120–300 mV s^{-1}. Inset: linear relationship between the peak currents and the square root of scan rates. **f** The relationship between the reduction peak potential and the Napierian logarithm of scan rate (lnv)

Au@Cu_2O-MIL-53(Fe)/GCE showed enhanced redox peak current owing to the high conductivity of AuNPs. Additionally, the electroactive surface area of different modified electrodes was calculated on the basis of the Randles-Sevcik equation.

$$Ip = 2.69 \times 10^5 n^{\frac{3}{2}} A D^{\frac{1}{2}} v^{\frac{1}{2}} C$$

where I_p refers to the peak current (A); n means the number of transition electrons of $[Fe(CN)_6]^{3-/4-}$ ($n = 1$); A is the effective surface area of electrode (cm^2); D refers to the diffusion coefficient, which is $(6.7 \pm 0.02) \times 10^{-6}$ cm^2 s^{-1}; ν means the scan rate (V s^{-1}); and C is the concentration of the redox reactant (5×10^{-6} mol cm^{-3}). The calculation result showed the tendency of MIL-53(Fe)/GCE (0.019 cm^2)<Cu_2O/GCE (0.034 cm^2)<Cu_2O-MIL-53(Fe)/GCE(0.073 cm^2) < Au@Cu_2O-MIL-53(Fe)/GCE (0.164 cm^2).

To explore the activity of Au@Cu_2O-MIL-53(Fe)/GCE towards the reduction of H_2O_2, CVs were operated in the absence and presence of H_2O_2 at a scan rate of 50 mV s^{-1} in N_2-saturated 0.01 M PBS (pH 7.4) (Fig. 3b–d). In the absence of H_2O_2, the CV curve displayed the character oxidation-reduction peaks of different materials, implying the composite material was successfully synthesized (Fig. 3b). With the addition of 5 mM H_2O_2, the curves of Cu_2O, MIL-53(Fe), and Cu_2O-MIL-53(Fe) only observed the light reduction peak current, but the curves of Au@Cu_2O-MIL-53(Fe)/GCE showed a typical electrocatalytic reaction behavior towards H_2O_2 (Fig. 3c). Furthermore, as the concentration of H_2O_2 increased, the reduction current was sharply enhanced, signifying an obvious electrocatalytic behavior to the reduction of H_2O_2 in a large concentration range (Fig. 3d). The mechanism of H_2O_2 reduction on Au@Cu_2O-MIL-53(Fe)/GCE was schematically shown in Scheme 1, which could be proposed that H_2O_2 was firstly reduced to H_2O by catalytic centers of Au^+; subsequently, the resulting Au^+ was transferred an electron to Au^0. Moreover, during this process, 2D porous structure of MIL-53(Fe) worked as a molecular sieve to enrich hydrogen peroxide improving the efficiency of the reaction with active sites, enhancing the catalytic process of H_2O_2.

To investigate the reaction kinetics, the electrochemical behavior of Au@Cu_2O-MIL-53(Fe)-modified electrode was studied by CV in 0.01 M PBS (pH 7.4) containing 5 mM H_2O_2 at different scan rates (Fig. 3e and f). The relationships of I~$v^{1/2}$ could be expressed as I(μA) = − 3.976 $V^{1/2}$(mVs^{-1})$^{1/2}$–49.691 ($R^2 = 0.997$), which was related to the diffusion-controlled process. Furthermore, the reduction (Epc) potential had a linear relationship with the natural logarithm of the scan rate (lnv).

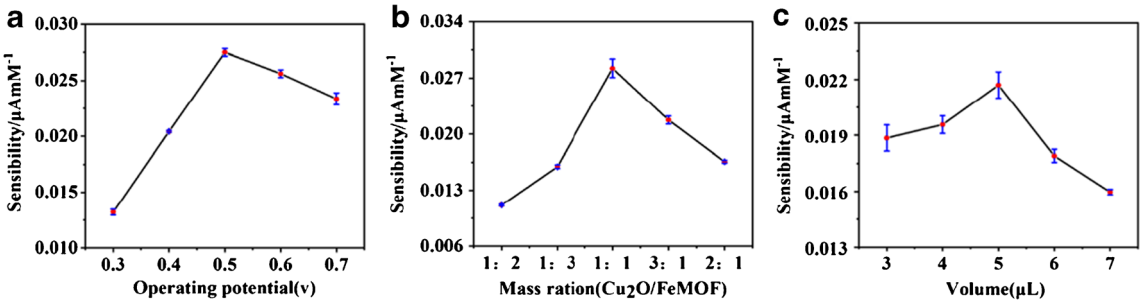

Fig. 4 Optimization study of **a** the applied potential, **b** different proportion of Cu_2O and MIL-53(Fe), and **c** the volume loading of Cu_2O-MIL-53(Fe) using IT curves with the successive addition of 100 μM H_2O_2 in N_2-saturated 0.01 M PBS (pH 7.4) under stirring at scan rate of 50 mVs^{-1}

The linear equations was $Epc = -0.044\ln v - 0.645$ with $R^2 = 0.998$, which follows Laviron's model [48].

$$Epc = E\theta + \frac{2.303RT}{\alpha nF}\ln v$$

where α is the electron transfer coefficient, n is the number of electron transfer, v is the scan rate, R is the gas constant, T is the absolute temperature, and F is the Faraday constant. From the slope of Ep vs. ln ν plot, the value of α was calculated to be 0.67 for electroreduction of H_2O_2.

Optimization of Au@Cu_2O-MIL-53(Fe)/GCE towards H_2O_2 reduction

To optimize the performance of Au@Cu_2O-MIL-53(Fe)/GCE, the applied potential, mass ratio of Cu_2O to MIL-53(Fe), and loading volumes were studied. The typical current-time (IT) was performed with the successive addition of 100 μM H_2O_2 in N_2-saturated 0.01 M PBS (pH 7.4) under stirring at scan rate of 50 mVs^{-1}. Figure 4a shows that the sensitivity varied with changing operating potential from − 0.3 to − 0.7 V. Sensitivity gradually increased at the beginning and decreased after reaching the peak, implying that − 0.5 V was the optimal potential. The Cu_2O could react with Fe^{3+} to bond on the surface of MIL-53(Fe). However, as Fe/Cu ratio increases, more Cu_2O was converted into CuO, which had a bad influence on the formation of AuNPs [37]. As shown in Fig. 4b, the effects of different proportions of Cu_2O and MIL-53 (Fe) on catalysis were studied. When the ratio of Cu_2O to MIL-53(Fe) was 1:1, the maximum response was obtained. Figure 4c shows that the maximum sensitivity was achieved when the sample volume was 5 μL. Excessive loading may lead to the aggregation of nanomaterials, which was a disadvantage to the sensitivity of the sensor. As a result, the combination of applied potential at − 0.5 V, the mass ratio of Cu_2O to MIL-53(Fe) at 1:1, and the loading volume of Cu_2O-MIL-53(Fe) at 5 μL were selected to establish the Au@Cu_2O-MIL-53(Fe)/GCE sensor.

Amperometric detection of H_2O_2 at Au@Cu_2O-MIL-53(Fe)/GCE

The electrochemical performance of the Au@Cu_2O-MIL-53(Fe)/GCE sensor was investigated using IT curves with successive addition of H_2O_2 to N_2-saturated 0.01 M PBS (pH 7.4)

Table 2 Performance comparison of various modified electrochemical H_2O_2 sensors

Electrode material	Linear range (μM)	Detection limit (μM)	Sensitivity (μA mM^{-1} cm^{-2})	Response time (s)	Ref.
AuNPs-NH_2/Cu-MOF	5–850	1.2	1.71	2	[49]
Ag-Au/Cu_2O	0–1400	1.30	0.416	–	[50]
RGO/Ag-Au/Cu_2O	50–50,750	0.10	1.4	–	[51]
Cu_2O/ERGO	1–1000	0.14	1682	–	[52]
3D Cu_2O-GA	1–1470	0.37	–	–	[53]
Au-Cu_xO_S	0.01–5.12	0.01	50.41	–	[54]
rGO-Pb NWs-Au NPs	5–1250	0.6	552.43	5	[55]
AuCu/SPCE	250–10,000	16.62	339.35	2–3	[56]
Au/Fe_3O_4	1–1000	266	0.108	5	[57]
RGO/Au/Fe_3O_4/Ag	2–12,000	–	1.43	2	[58]
Co_3O_4	0.4–2200	0.105	120.55	3	
Au@Cu_2O-MIL-53(Fe)	10–1520	1.01	351.57	3	This work

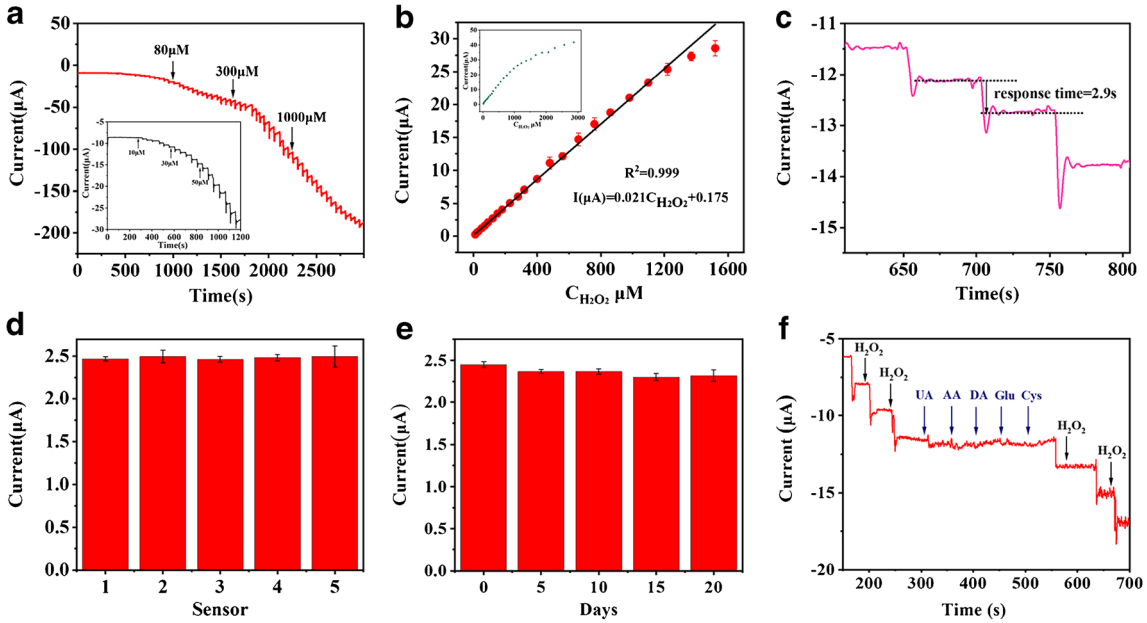

Fig. 5 **a** Amperometric current change of Au@Cu_2O-MIL-53(Fe)/GCE to continuous additions of different concentration of H_2O_2 to N_2-saturated 0.01 M PBS (pH 7.4) under stirring with optimal conditions in every 50 s at scan rate of 50 mVs^{-1} at − 0.5 V. **b** The linear fitting relationship between the current response and H_2O_2 concentrations in the range of 10 to 1520 μM. Inset: Current responded to the H_2O_2 concentrations. **c** The current response time, **d** reproducibility, **e** stability, and **f** selectivity of Au@Cu_2O-MIL-53(Fe)/GCE biosensor using IT curves with the successive addition of 100 μM H_2O_2 in N_2-saturated 0.01 M PBS (pH 7.4) under stirring at scan rate of 50 mVs^{-1} at − 0.5 V

under stirring (Fig. 5a) with optimal conditions at scan rate of 50 mVs^{-1}. Plotting the data of current response and H_2O_2 concentrations, there was a linear trend from 10 to 1520 μM, which was expressed as $I(\mu A) = 0.021C_{H2O2}(\mu M) + 0.175$ (R^2 = 0.999) (Fig. 5b) with a low detection limit of 1.01 μM (S/*N* = 3) and large detection sensitivity of 351.57 $\mu A \mu M^{-1}$ cm^{-2}. Meanwhile, the response time was less than 3 s (Fig. 5c). As shown in Table 2, the performance of this biosensor was better than those of Ag-Au/Cu_2O(45), graphene nanocomposites(47), or Ag/Cu-TCPP(50).

The reproducibility, stability, and selectivity of the Au@Cu_2O-MIL-53(Fe)/GCE sensor was confirmed by the continuous addition of 100 μM H_2O_2 under the same conditions. The relative standard deviation (RSD) of five different sensors was 1.7%, indicating the excellent reproducibility (Fig. 5d). And the current response maintained 98.5% within 20 days, implying the good stability (Fig. 5e). Anti-interference ability was another significant standard of practical application. As shown in Fig. 5f, no obvious current response was found when other biological metabolites were added, such as uric acid (UA), ascorbic acid (AA), dopamine hydrochloride (DA), cysteine (Cys), and glucose (Glu), confirming the excellent selectivity of the sensor.

Real-time monitoring of H_2O_2 released from living cells

Firstly, standard spiked recovery experiments were carried out to verify the feasibility of the Au@Cu_2O-MIL-53(Fe)/GCE sensor. Standard H_2O_2 at 50, 100, and 200 μM was added to the diluted 30-fold human serum sample in N_2-saturated 0.01 M PBS (pH 7.4) with optimal conditions at scan rate of 50 mVs^{-1}. The high recovery results of 97.68 to 102.75% (ESM Table. S1) implied that the Au@Cu_2O-MIL-53(Fe)/

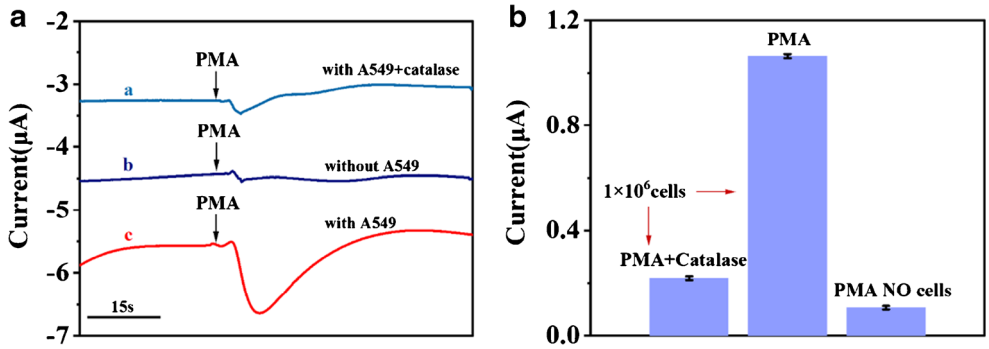

Fig. 6 **a** Amperometric response to real-time detection of H_2O_2 released from living human lung cancer A549 cells stimulated by PMA at − 0.5 V. **b** Plots of amperometric response corresponding to curve a, b, and c

Table 3 The estimation of H_2O_2 released from each cell based on electrochemical sensors

Electrode material	Sample	Concentration/ cell	Ref.
AuPd-PDA	Raw 264.7 cells HeLa cells	1.1 pM 0.8 pM	[20]
Mb@$MnMoSe_2$	HaCaT cells RAW 264.7	0.12 pM 0.1 pM	[22]
Nafion/PB-ERGO	Living cells	18.3 fM	[23]
Au@C-Co_3O_4	HKC cells HeLa cells MCF-7 cells	1.32 pM 2.06 pM 2.38 pM	[24]
Fe_3O_4/3DG NCs	A549 cells	0.091 fM	[60]
CS-SGO@HKUST-1	Raw 264.7 Cells	2.8 pM	[61]
Au@Cu_2O-MIL-53(Fe)	A549 cells	0.042 fM	This work

GCE electrochemical sensor had practical applications for H_2O_2 detection in a real sample.

Furthermore, the Au@Cu_2O-MIL-53(Fe)/GCE electrochemical sensor was applied to real-time monitor the H_2O_2 released from living human lung cancer A549 cells. Here, IT curves were used with successive addition of PMA to N_2-saturated 0.01 M PBS (pH 7.4) in the absence and presence of cell A549 or catalase with optimal conditions at scan rate of 50 mVs^{-1}(Fig. 6). PMA was chosen to stimulate the intracellular protein kinase C (pKC) activation, resulting in H_2O_2 secretion of cells in situ [59]. The catalase was used to selectively decompose the H_2O_2 released by PMA stimulation. As shown in Fig. 6a, there was only a small current change when PMA was added in the absence of cells (curve b). When 1.0×10^6 cells were treated with 10 μL of 200 ng mL^{-1} PMA, the current increased sharply (curve c). However, the current response becomes gentle in the presence of cells and catalase (curve a). Moreover, the current responses were 1.06 μA, corresponding to 42.23 μM H_2O_2 released from the cells. From this calculation, the amount of H_2O_2 released by a single cell was 0.042 fmol.

A comparison of our design electrochemical sensors with those reported in researches about the estimation of H_2O_2 released from living cell was shown in Table 3. As shown, the modified electrode showed excellent sensitivity and electrocatalytic activity towards trace H_2O_2 released from living cells. However, compared with other sensors, it detected a smaller amount of H_2O_2 released by a single cell, which may be limited by the used PMA concentration. The

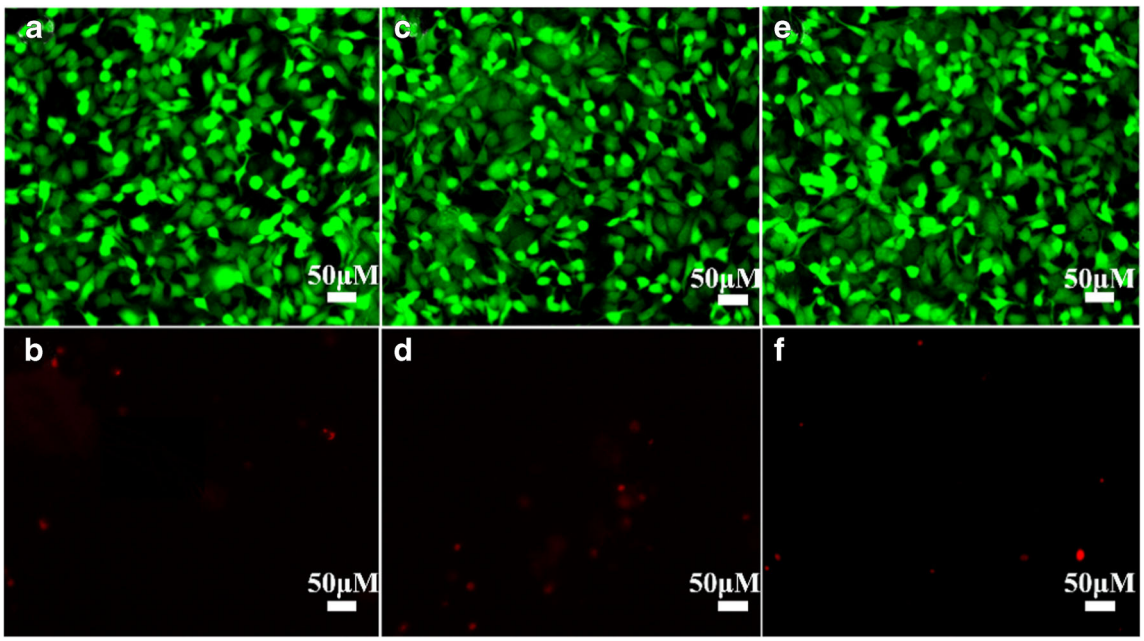

Fig. 7 Fluorescence imaging of A549 cells cultured with different situations as stained by Calcein-AM (green) and PI (red). **a** and **b** were cultured with normal physiological condition. **c** and **d** were cultured with Au@Cu_2O-MIL-53(Fe) for 24 h labeled. **e** and **f** were cultured with 200 ng/mL PMA for 15 min

outstanding performance of the modified electrode in monitoring H_2O_2 released from cells was mainly contributed by the synergistic catalysis of MOF and MNPs. The 2D sheet structure of MIL-53(Fe) could provide attachment sites for MNPs and enrich the concentration of trace H_2O_2 released from cells. Besides, the Au@Cu_2O-MIL-53(Fe) grown on the surface of MOF framework allowed the direct contact with H_2O_2 with decreasing diffusion resistance in the electrocatalytic reaction.

To prove the detection results of Au@Cu_2O-MIL-53(Fe)/GCE electrochemical sensor for H_2O_2 released of cells with the PMA stimulation, cell staining experiments were carried out in 6-well clear TC-treated multiple well plates for 24 h in 3 mL 0.01 M PBS (pH 7.4) containing 1×10^{-6} A549 cells (Fig. 7). The cells will be stained by Calcein-AM (green) and PI (red), corresponding to live and dead cells, respectively. As can be seen in Fig. 7a and b, cells grew well and there were few dead cells under normal physiological condition. The cell biocompatibility of Au@Cu_2O-MIL-53(Fe) towards A549 cells was investigated by co-culture 10 μg mL^{-1} of nanomaterials with cells for 24 h. Compared with the normal physiological condition, the cells still grow well, revealing the good cell biocompatibility of Au@Cu_2O-MIL-53(Fe) (Fig. 7c and d). In addition, all the electrochemical measurements of H_2O_2 released from the living cells were operated within 30 min, so the survival state of the cells was observed after the addition of 200 ng/mL PMA for the same time. As shown in Fig. 7e and f, the cells were still alive after adding the PMA for 30 min, proving that A549 cells have good bioactivity during electrochemical testing.

These results further illustrated that the Au@Cu_2O-MIL-53(Fe)/GCE non-enzymatic electrochemical biosensor possessed practically the potential for the real-time detection of H_2O_2.

Conclusion

A flower-like heterogeneous nanosphere Au@Cu_2O-MIL-53(Fe) was prepared through electrodeposition of Au nanoparticles onto Cu_2O-MIL-(Fe) assembled by redox in advance. Characterization analysts of FE-SEM, TEM, XRD, and XPS demonstrated that the Cu_2O played a critical role for AuNP growth uniform and attached to the outside skeleton of MIL-53(Fe) sheets. And one-step low potential deposition strategy was applied to reduce the metal ions to a metal-type solid state, enhancing the electrochemical performance of Au@Cu_2O-MIL-53(Fe). Benefiting from the excellent conductivity and catalyst durability, the Au@Cu_2O-MIL-53(Fe)/GCE non-enzymatic electrochemical sensor showed fast response and excellent anti-interference high current response towards H_2O_2 reduction. Based on these features, the constructed sensor was successfully used for the real-time detection of the H_2O_2 released from living cancer cells. Meanwhile, the result of confocal fluorescence microscopy verified the survival of cells during the detection process. The as-reported work complemented the strategy of assembling MNPs on MOF and opened an avenue for non-enzymatic electrochemical sensor in biological samples.

Funding This work was supported by the National Natural Science Foundation of China (NO. 81772290), Graduate Scientific Research and Innovation Foundation of Chongqing, China (Grant No.CYB20070, CYS2007), Chongqing science and technology commission (CSTC2018jcyjAX0062), Chongqing Graduate Tutor Team Construction Project, Analytical and Testing Center of Chongqing University for (SEM/TEM/the characterization of EDS/XRD/XPS), and the sharing fund of Chongqing University's large equipment.

Compliance with ethical standards

Conflict of interest The authors declare that they have no competing interests.

References

1. Dong Z, Yang Zj, Hao Y, Feng L. Fabrication of H_2O_2-driven nanoreactors for innovative cancer treatments. Nanoscale. 2019;11:16164–86.
2. Lim CK, Lee YD, Na J, Oh JM, Song H, Kim K, et al. Chemiluminescence-generating nanoreactor formulation for near-infrared imaging of hydrogen peroxide and glucose level in vivo. Adv Funct Mater. 2010;20(16):2644–8.
3. Qiao J, Liu Z, Tian Y, Wu M, Niu Z. Multifunctional self-assembled polymeric nanoprobes for FRET-based ratiometric detection of mitochondrial H_2O_2 in living cells. Chem Commun. 2015;51(17):3641–4.
4. Zhou H, Liu J, Zhang S. Quantum dot-based photoelectric conversion for biosensing applications. TrAC Trends Anal Chem. 2015;67:56–73.
5. Abbas K, Hardy M, Poulhès F, Karoui H, Tordo P, Ouari O, et al. Detection of superoxide production in stimulated and unstimulated living cells using new cyclic nitrone spin traps. Free Radic Biol Med. 2014;71:281–90.
6. Chen W, Cai S, Ren Q-Q, Wen W, Zhao Y-D. Recent advances in electrochemical sensing for hydrogen peroxide: a review. Analyst. 2012;137(1):49–58.
7. Meng L, Jin J, Yang G, Lu T, Zhang H, Cai C. Nonenzymatic electrochemical detection of glucose based on palladium-single-walled carbon nanotube hybrid nanostructures. Anal Chem. 2009;81(17):7271–80.
8. Li M, Wu J, Su H, Tu Y, Shang Y, He Y, et al. Ionic liquid-polypyrrole-gold composites as enhanced enzyme immobilization platforms for hydrogen peroxide sensing. Sensors. 2019;19(3):6402.
9. Kong Y-T, Boopathi M, Shim Y-B. Direct electrochemistry of horseradish peroxidase bonded on a conducting polymer modified glassy carbon electrode. Biosens Bioelectron. 2003;19(3):227–32.
10. Li L, Wang X, Liu G, Wang Z, Wang F, Guo X, et al. Reproducible preparation of a stable polypyrrole-coated-silver nanoparticles decorated polypyrrole-coated-polycaprolactone-nanofiber-based cloth electrode for electrochemical sensor application. Nanotechnology. 2015;26(44):445704.
11. Zhang W, Wang C, Guan L, Peng M, Li K, Lin Y. A non-enzymatic electrochemical biosensor based on Au@PBA(Ni-Fe): MoS nanocubes for stable and sensitive detection of hydrogen

peroxide released from living cells. J Mater Chem B. 2019;7(48):7704–12.
12. Zhao W, Jin J, Wu H, Wang S, Fneg C, Yang S, et al. Electrochemical hydrogen peroxide sensor based on carbon supported Cu@Pt core-shell nanoparticles. Mater Sci Eng C Mater Biol Appl. 2017;78:185–90.
13. Li C, Chen D, Wang Y, Lai X, Peng J, Wang X, et al. Simultaneous electrochemical detection of nitrite and hydrogen peroxide based on 3D Au-rGO/FTO obtained through a one-step synthesis. Sensors. 2019;19(6):1304.
14. Sun Y, Luo M, Meng X, Xiang J, Wang L, Ren Q, et al. Graphene/intermetallic PtPb nanoplates composites for boosting electrochemical detection of H_2O_2 released from cells. Anal Chem. 2017;89(6):3761–7.
15. Bai J, Jiang X. A facile one-pot synthesis of copper sulfide-decorated reduced graphene oxide composites for enhanced detecting of H_2O_2 in biological environments. Anal Chem. 2013;85(17):8095–101.
16. Du X, Chen Y, Dong W, Han B, Liu M, Chen Q, et al. A nanocomposite-based electrochemical sensor for non-enzymatic detection of hydrogen peroxide. Oncotarget. 2017;8(8):13039–47.
17. Zhou Y, Li C, Hao Y, Ye B, Xu M. Oriented growth of cross-linked metal-organic framework film on graphene surface for non-enzymatic electrochemical sensor of hydrogen peroxide in disinfectant. Talanta. 2018;188:282–7.
18. Wang C, Zhou M, Ma Y, Tan H, Wang Y, Li Y. Hybridized polyoxometalate-based metal-organic framework with Ketjenblack for the nonenzymatic detection of H_2O_2. Chem Asian J. 2018;13(16):2054–9.
19. Ling W, Hao Y, Fau-Wang H, Wang H, Fau-Xu H, Xu H, et al. A novel Cu-metal-organic framework with two-dimensional layered topology for electrochemical detection using flexible sensors. Nanotechnology. 2019;30(42):424002.
20. He G, Gao F, Li W, Li P, Zhang X, Yin H, et al. Electrochemical sensing of H_2O_2 released from living cells based on AuPd alloy-modified PDA nanotubes. Anal Methods. 2019;11(12):1651–6.
21. Zhu L, Zhang Y, Xu P, Wen W, Li X, Xu J. PtW/MoS_2 hybrid nanocomposite for electrochemical sensing of H_2O_2 released from living cells. Biosens Bioelectron. 2016;80:601–6.
22. Ramaraj S, Sakthivel M, Chen SM, Lou BS, Ho KC. Defect and additional active sites on the basal plane of manganese-doped molybdenum diselenide for effective enzyme immobilization: in vitro and in vivo real-time analyses of hydrogen peroxide sensing. ACS Appl Mater Interfaces. 2019;11(8):7862–71.
23. Qiu W, Zhu Q, Gao F, Gao F, Huang J, Pan Y, et al. Graphene oxide directed in-situ synthesis of Prussian blue for non-enzymatic sensing of hydrogen peroxide released from macrophages. Mater Sci Eng C Mater Biol Appl. 2017;72:692–700.
24. Dai H, Chen Y, Niu X, Pan C, Chen H, Chen X. High-performance electrochemical biosensor for nonenzymatic H_2O_2 sensing based on Au@C-Co_3O_4 heterostructures. Biosens Bioelectron. 2018;118:36–43.
25. Yaghi OM, O'Keeffe M, Ocking NW, Chae HK, Eddaoudi M, et al. Reticular synthesis and the design of new marterials. Nature. 2003;423:705–14.
26. Fu Y, Dai J, Ge Y, Zhang Y, Ke H, Zhang W. A novel non-enzymatic electrochemical hydrogen peroxide sensor based on a metal-organic framework/carbon nanofiber composite. Molecules. 2018;23(10):2552.
27. Feng J, Wang H, Ma Z. Ultrasensitive amperometric immunosensor for the prostate specific antigen by exploiting a Fenton reaction induced by a metal-organic framework nanocomposite of type Au/Fe-MOF with peroxidase mimicking activity. Mikrochim Acta. 2020;187(1):95.
28. Ling P, Qian C, Yu J, Gao F. Artificial nanozyme based on platinum nanoparticles anchored metal-organic frameworks with enhanced electrocatalytic activity for detection of telomeres activity. Biosens Bioelectron. 2020;149:111838.
29. Chen C, Xiong D, Gu M, Lu C, Yi F-Y, Ma X. MOF-derived bimetallic CoFe-PBA composites as highly selective and sensitive electrochemical sensors for hydrogen peroxide and nonenzymatic glucose in human serum. ACS Appl Mater Interfaces. 2020;12(31):35365–74.
30. Horike S, Dinca M, Tamaki K. Long JRJJotACS. Size-selective Lewis acid catalysis in a microporous metal-organic framework with exposed Mn^{2+} coordination sites. J Am Chem Soc. 2008;130(18):5854–5.
31. Devic T, Horcajada P, Serre C, et al. Functionalization in flexible porous solids: effects on the pore opening and the host-guest interactions. J Am Chem Soc. 2010;132(3):1127–36.
32. Ma J, Bai W, Zheng J. Non-enzymatic electrochemical hydrogen peroxide sensing using a nanocomposite prepared from silver nanoparticles and copper (II)-porphyrin derived metal-organic framework nanosheets. Mikrochim Acta. 2019;186(7):482.
33. Pan Y, Yuan B, Li Y, He D. Multifunctional catalysis by Pd@MIL-101: one-step synthesis of methyl isobutyl ketone over palladium nanoparticles deposited on a metal-organic framework. Chem Commun (Camb). 2010;46(13):2280–2.
34. Huang Y, Lin Z, Cao R. Palladium nanoparticles encapsulated in a metal-organic framework as efficient heterogeneous catalysts for direct C_2 arylation of indoles. Chemistry. 2011;17(45):12706–12.
35. Zhao M, Deng K, He L, Liu Y, Li G, Zhao H, et al. Core-shell palladium nanoparticle@metal-organic frameworks as multifunctional catalysts for cascade reactions. J Am Chem Soc. 2014;136(5):1738–41.
36. Szécsényi Á, Li G, Gascon J, Pidko EA. Unraveling reaction networks behind the catalytic oxidation of methane with H_2O_2 over a mixed-metal MIL-53(Al,Fe) MOF catalyst. Chem Sci. 2018;9(33):6765–73.
37. Li H, Ban L, Niu Z, Huang X, Meng P, Han X, et al. Application of CuxO-FeyOz nanocatalysts in ethynylation of formaldehyde. Nanomaterials (Basel). 2019;9(9):1301.
38. Liang Y, Chen Z, Yao W, Wang P, Yu S, Wang X. Decorating of Ag and CuO on cu nanoparticles for enhanced high catalytic activity to the degradation of organic pollutants. Langmuir. 2017;33(31):7606–14.
39. Zhu XD, Wang KX, Yan DJ, Le SR, Ma RJ, Sun KN, et al. Creating a synergistic interplay between tubular MoS_2 and particulate Fe_3O_4 for improved lithium storage. Chem Commun (Camb). 2015;51(59):11888–91.
40. Liang R, Jing F, Shen L, Qin N. Wu LJJoHM. MIL-53(Fe) as a highly efficient bifunctional photocatalyst for the simultaneous reduction of Cr(VI) and oxidation of dyes. J Hazard Mater. 2015;287C:364–72.
41. Wang C, Zhang Y, Li Y, Liu J, Wu QH, Jiang J, et al. Synthesis of fluorine-doped α-Fe2O3 nanorods toward enhanced lithium storage capability. Nanotechnology. 2017;28(6):065401.
42. Biesinger MC, Payne BP, Grosvenor AP, Lau LWM, Gerson AR, Smart RSC. Resolving surface chemical states in XPS analysis of first row transition metals, oxides and hydroxides: Cr, Mn, Fe, Co and Ni. Appl Surf Sci. 257(7):2717–30.
43. Luo J, Liu Y, Niu Y, Jiang Q, Huang R, Zhang B, et al. Insight into the chemical adsorption properties of CO molecules supported on Au or Cu and hybridized Au-CuO nanoparticles. Nanoscale. 2017;9(39):15033–43.
44. Bulushev DA, Yuranov I, Suvorova EI, Buffat PA, Kiwi-Minsker L. Highly dispersed gold on activated carbon fibers for low-temperature CO oxidation. J Catal. 2004;224(1):8–17.
45. Yang M, Allard LF. Flytzani-Stephanopoulos MJJotACS. Atomically dispersed Au-(OH) x species bound on titania catalyze the low-temperature water-gas shift reaction. J Am Chem Soc. 2013;135(10):3768–71.

46. Yang Q, Jiang H-L. Oxidation or reduction state of Au stabilized by an MOF: active site identification for the three-component coupling reaction. Small Methods. 2018;2:1800216.
47. Yang P, Pan J, Liu Y, Zhang X, Feng J, Hong S, et al. Insight into the role of unsaturated coordination O_2c-Ti_5c-O_2c sites on selective glycerol oxidation over AuPt/TiO_2 catalysts. ACS Catal. 2018;9(1):188–99.
48. Daemi S, Ghasemi S, Akbar Ashkarran A. Electrospun CuO-ZnO nanohybrid: tuning the nanostructure for improved amperometric detection of hydrogen peroxide as a non-enzymatic sensor. J Colloid Interface Sci. 2019;550:180–9.
49. Dang W, Sun Y, Jiao H, Xu L, Lin M. AuNPs-NH_2/cu-MOF modified glassy carbon electrode as enzyme-free electrochemical sensor detecting H_2O_2. J Electroanal Chem. 2020;856:113592.
50. Li D, Meng L, Dang S, Jiang D, Shi W. Hydrogen peroxide sensing using Cu_2O nanocubes decorated by Ag-Au alloy nanoparticles. J Alloys Compd. 2017;690:1–7.
51. Li D, Meng L, Xiao P, Jiang D, Dang S, Chen M. Enhanced non-enzymatic electrochemical sensing of hydrogen peroxide based on Cu_2O nanocubes/Ag-Au alloy nanoparticles by incorporation of RGO nanosheets. J Electroanal Chem. 2017;791:23–8.
52. Doğan HÖ, Çepni E, Urhan BK, Eryiğit M. Non-enzymatic amperometric detection of H_2O_2 on one-step electrochemical fabricated Cu_2O/electrochemically reduced graphene oxide nanocomposite. Chem Select. 2019;4(28):8317–21.
53. Cheng C, Zhang C, Gao X, Zhuang Z, Du C, Chen W. 3D network and 2D paper of reduced graphene oxide/CuO composite for electrochemical sensing of hydrogen peroxide. Anal Chem. 2018;90(3):1983–91.
54. Zhou L, Kuai L, Li W, Geng B. Ion-exchange route to Au-$Cu(_x)O_S$ yolk-shell nanostructures with porous shells and their ultrasensitive H_2O_2 detection. ACS Appl Mater Interfaces. 2012;4(12):6463–7.
55. Dong W, Ren Y, Zhang Y, Chen Y, Zhang C, Bai Z, et al. Synthesis of Pb nanowires-au nanoparticles nanostructure decorated with reduced graphene oxide for electrochemical sensing. Talanta. 2017;165:604–11.
56. Ngamaroonchote A, Sanguansap Y, Wutikhun T, Karn-Orachai K. Highly branched gold-copper nanostructures for non-enzymatic specific detection of glucose and hydrogen peroxide. Mikrochim Acta. 2020;187(10):559.
57. Liu H, Chen Q, Cheng X, Wang Y, Zhang Y, Fan G. Sustainable and scalable in-situ fabrication of Au nanoparticles and Fe_3O_4 hybrids as highly efficient electrocatalysts for the enzyme-free sensing of H_2O_2 in neutral and basic solutions. Sensors Actuators B Chem. 2020;314:128067.
58. Heydaryan K, Kashi M, Sharifi N, Ranjbar-Azad M. Efficiency improvement in non-enzymatic H_2O_2 detection induced by the simultaneous synthesis of Au and Ag nanoparticles in an RGO/Au/Fe_3O_4/Ag nanocomposite. New J Chem. 2020;44(21):9037–45.
59. Takatoshi T, Hitomi O, Katsuyuki M, Ryokei O, Chiyoko I. Phorbol 12-myristate 13-acetate (PMA)-induced oxyradical production in rheumatoid synovial cells. Jpn J Pharmacol. 1997;73:347–51.
60. Zhao Y, Huo D, Bao J, Yang M, Chen M, Hou J, et al. Biosensor based on 3D graphene-supported Fe_3O_4 quantum dots as biomimetic enzyme for in situ detection of H_2O_2 released from living cells. Sensors Actuators B Chem. 2017;244:1037–44.
61. Wang Q, Yang Y, Gao F, Ni J, Zhang Y, Lin Z. Graphene oxide directed one-step synthesis of flowerlike graphene@HKUST-1 for enzyme-free detection of hydrogen peroxide in biological samples. ACS Appl Mater Interfaces. 2016;8(47):32477–87.